NJC

ROYAL SOCIETY OF CHEMISTRY

PAPER

Cite this: *New J. Chem.*, 2023, **47**, 14885

Reverse voltage pulse deposition of a porous polyaniline/Mn–Co sulfide composite cathode material for modified Zn-ion hybrid supercapacitors†

Duong V. Thiet,[a] Doan T. Tung,*[bc] Le T. T. Tam,[bc] Ngo T. Dung,[b] Le T. Tam,[d] Pham T. Nam,[b] Nguyen T. T. Trang,[b] Dimitra Vernardou,[e] Top K. Le,[fg] Nguyen V. Tam,[h] Tran D. Lam[bc] and Le T. Lu*[bc]

Received 28th April 2023,
Accepted 29th June 2023

DOI: 10.1039/d3nj01962d

rsc.li/njc

For the purpose of expanding the working potential window and reducing the self-discharge for a Zn-ion hybrid supercapacitor, a positive electrode (cathode) of the Mn–Co-sulfide–polyaniline (MCS–PANi) composite coated on porous graphite paper was prepared using the reverse voltage pulse electrodeposition method. The electrode first achieved a high specific capacitance of 1048.8 F g^{-1} at a scan rate of 5 mV s^{-1} in the 1 M $ZnSO_4$ and 0.1 M $MnSO_4$ electrolyte solution. The Zn negative electrode (anode) was modified by organic fatty alcohol additives to reduce oxidation and dendrite growth. A hydrophilic modified polypropylene (PP) nonwoven fabric was used as a separator. The MCS–PANi-Zn-ion hybrid supercapacitor (MPZHSC) exhibited a very wide potential window of 2 V in aqueous electrolytes, a high specific capacitance value of 586.7 F g^{-1} at a scan rate of 5 mV s^{-1}, an excellent durability of 98.3% after 11 232 cycles and a low self-discharge rate, retaining over 60% of its initial voltage value after 7 days. In addition, a device with a small active area of 2 cm^2 can be used to light a 2.5 W LED module for about 15 min, suggesting MPZHSC's potential practical applications.

Introduction

In recent years, portable electronic devices and electric vehicles have been rapidly developed requiring higher demands for energy and power density, safety, and low cost of electrochemical energy storage devices.[1,2] Research on battery technologies such as Pb–acid, Ni–Cd, Na–S and particularly Li-ion batteries (LIBs) is on a continuous progress towards this direction.[3] Up to date, LIBs have achieved great success and been widely used in practice. A huge increase in annual production of LIBs has as a consequence of the depletion of lithium raw materials and high cost of the battery system.[4] Recently, sodium-ion batteries (SIBs) and potassium-ion batteries (PIBs) have been also developed as alternatives for LIBs due to their abundant and relatively low cost.[5–7] Nevertheless, LIBs, SIBs, and PIBs have relatively low durability and safety.

Rechargeable supercapacitors have recently garnered increasing attention from scientists. However, they have some major disadvantages, which are high self-discharge, a low working voltage and a voltage drop during their operation. The self-discharge rate in a supercapacitor is much greater than that in a battery; in a conventional supercapacitor, the voltage drops by about 40% after 12 hours.[8] This is a serious drop because supercapacitors are mainly used in the first half of the active potential window. At the same time, the potential window of a supercapacitor based on an environmentally friendly aqueous electrolyte solution usually only reaches the limit of 1.2 V due to the occurrence of electrolysis, and even when using an organic electrolyte solution, the working potential on many supercapacitor products currently on the market is only 2.7 V.[9] Therefore, when the potential of a supercapacitor decreases rapidly, the energy density proportional to the square of the potential and the potential is significantly lowered, which

[a] *Faculty of Mechanical Engineering, Hanoi University of Industry, Tu Liem District, Hanoi, Vietnam*
[b] *Institute for Tropical Technology-Vietnam Academy of Science and Technology (VAST), 18 Hoang Quoc Viet, Hanoi, Vietnam. E-mail: dtungtnt167@gmail.com, ltlu@itt.vast.vn*
[c] *Graduate University of Science and Technology-VAST, 18 Hoang Quoc Viet, Hanoi, Vietnam*
[d] *Vinh University, 182 Le Duan, Vinh City, Nghe An, Province 43000, Vietnam*
[e] *Department of Electrical and Computer Engineering, School of Engineering, Hellenic Mediterranean University, 71410 Heraklion, Greece*
[f] *Faculty of Materials Science and Technology, University of Science, Ho Chi Minh City 700000, Vietnam*
[g] *Vietnam National University, Ho Chi Minh City 700000, Vietnam*
[h] *Defect Control Group, Samsung Display Vietnam Co., Ltd, Yen Phong Industrial Zone, Yen Trung, Yen Phong, Bac Ninh, Vietnam*

† Electronic supplementary information (ESI) available. See DOI: https://doi.org/10.1039/d3nj01962d

will be a key point that greatly affects the practical application of supercapacitors. For the purpose of overcoming the above disadvantages, the studied hybrid supercapacitors have shown better properties such as a wide working potential, low self-discharge, and higher energy and power densities. Several types of battery-hybrid supercapacitors using metal ions (Li^+, Na^+, K^+, Zn^{2+}, Mg^{2+}, Ca^{2+}, and Al^{3+}) have been developed to improve the durability, energy and power density of the devices.[10–21] Among these, multivalent metal ions (*e.g.*, Zn^{2+}, Mg^{2+}, Ca^{2+}, and Al^{3+}) may possess some distinct advantages, such as a high capacity and energy density compared with univalent metal ions (Li^+, Na^+, K^+, *etc.*)[22] These happen because a multivalent cation can transfer twice or three times more electrons to the electrode, providing a high charge-transfer efficiency and an overall enhanced supercapacitor performance.

The zinc-ion hybrid supercapacitor (ZHSC) is a promising system as the zinc metal is an available and cheap material. Zn ions are also suitable for aqueous electrolytes due to their low redox potential (−0.76 V *vs.* standard hydrogen electrode (SHE)) and high overpotential for hydrogen evolution with a satisfactory theoretical capacity of 820 mA h g^{-1} (5855 mA h cm^{-3}) for the Zn electrode.[23–26] The positive electrode of the Zn-ion hybrid supercapacitor is usually based on carbon materials with a large specific surface area.[27–30] However, the main issue of carbon-based electrode materials is the low specific capacitance and lower energy density. The plan to introduce the pseudo-capacitive effect into anode materials is also being directed. Compared with carbon materials, pseudo-capacitive materials contribute a greater capacity to the energy storage device. The combination of pseudo-capacitive materials will be a promising research trend for Zn-ion hybrid supercapacitors. However, the number of publications is still limited.

Besides, the Zn negative electrode during the working process often tends to form uncontrolled dendrites. This is combined with the low mobility of the Zn^{2+} ion, leading to a decrease of the cycling lifespan and Coulomb efficiency of ZHSCs. Recently, various functional materials, such as reduced graphene oxide (rGO), active carbon, carbon black, TiO_2, and porous nano-$CaCO_3$, have been reported as protective layers to restrain the dendrite growth, gas evolution, and by-product formation.[31–35] Chet *et al.* investigated the effect of organic/inorganic additives (such as cetyltrimethylammonium bromide, sodium dodecyl sulfate, polyethylene–glycol, thiourea indium sulfate, tin oxide, and boric acid) on electrode protective layers. The findings reveal that these additives affect the different crystallographic orientations and surface textures of zinc anodes, resulting in 6–30 times less corrosion of zinc anodes in the aqueous electrolyte than without additive ones.[36,37]

Regarding the electrode materials based on transition-metal sulfides and conducting polymers, they have shown to contribute high specific capacitances.[38–41] However, metal sulfide compounds often exhibit good electrochemical properties in supercapacitor systems using alkaline electrolyte solutions (*e.g.* KOH, NaOH). Therefore, metal sulfide materials have hardly been studied in electrolyte solutions of zinc ion batteries such as $ZnSO_4$.

In this work, the electrochemical deposition method was used to fabricate the cathode of Mn–Co-sulfide and polyanilne composite materials for Zn-ion hybrid supercapacitors. The zinc anode was plated in the presence of organic fatty alcohol additives. The cathode and anode were then reassembled into a full cell ZHSC using a hydrophilic treated PP non-woven fabric separator and 1 M $ZnSO_4$–0.1 M $MnSO_4$ electrolyte solution. The characterisation results demonstrated high features for the SC electrodes, including high capacitance and durability. In particular, the MCS–PAN composite material has achieved good electrochemical properties in non-alkaline aqueous electrolyte solutions while contributing to widening the potential window for Zn-ion hybrid supercapacitors up to 2 V. An MPZHSC with only a small active area of 2 cm^2 exhibited a relatively low self-discharge rate with retaining over 60% of its initial voltage value after 7 days, and it was able to illuminate a 2.5 W LED module for about 15 min.

Experimental section

Materials

Manganese(II) sulfate monohydrate 99%, cobalt(II) sulfate heptahydrate 99%, aniline, zinc sulfate heptahydrate 99%, thiourea, zinc foil and ethanol were purchased from Sigma-Aldrich Ltd, Singapore. Alcohol ethoxylate $C_{12}H_{25}O{\cdot}(C_2H_4O)_n$ was ordered from Shanghai Zhanyun Chemical Co., Ltd. Graphite paper was supplied by Xiamen Tob New Energy Technology Co., Ltd. This graphite paper has a porosity of 75%, and it is cleaned by ultrasonic vibration in alcohol before use. Nonwoven polypropylene (PP) fabric was received from Bignano Ltd. Co (Vietnam). All other chemicals were used as received without any further purification.

Fabrication of ZHSCs

Cathode. The Mn–Co-sulfide–polyaniline (MCS–PANi) composites were deposited onto a graphite paper serving as both electrodes. After the cleaning and drying process, the graphite paper was covered with plastic glue for fixing an active surface area. The electrodeposition experiments were performed in an aqueous solution consisting of 7 mM $Co(SO_4){\cdot}7H_2O$, 7 mM $Mn(SO_4){\cdot}H_2O$, 0.7 M thiourea and 0.1 M aniline. The sulphate salts and thiourea were added, and the substrate was stirred (with its half area immersed in the electrolyte being 1 × 2 cm^2) using the voltage pulse technique. The electrochemical system consists of two electrodes in which the graphite paper is used until complete dissolution to a homogeneous solution with a light-pink color. Then, aniline was slowly added using a micropipette. The voltages were applied in the range of 1.5 V to −1.5 V alternatively for 100 s and repeated 4 times (Scheme 1). Next, the positive and negative electrodes were interchanged, and the procedure was carried out one more time.

Anode. The plating solution was prepared on a heated magnetic stirrer. Double-distilled water was heated to 60 °C. Fatty alcohol ethoxylate (2 ml) was then gradually dissolved in double-distilled water with continuous magnetic stirring.

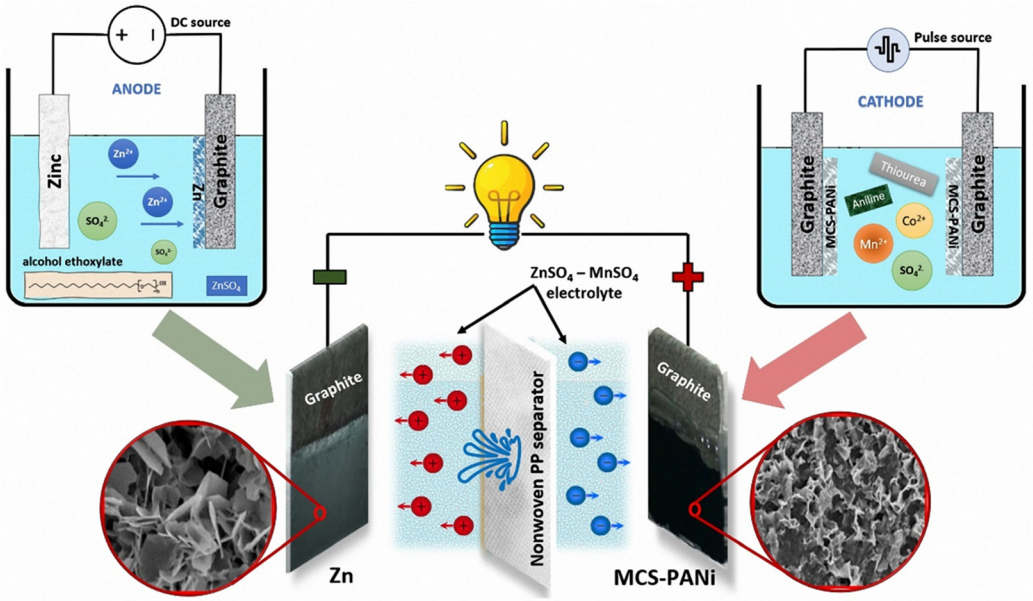

Scheme 1 Process for fabrication of the MCS–PANi Zn-ion hybrid supercapacitor (MPZHSC).

When the solution became homogeneous, the $ZnSO_4$ salt was added slowly so that the concentration remained at 2 M. The beginning voltage of 1 V was maintained for 30 s and then increased to 1.8 V and kept for 330 s (Fig. S1b, ESI†) for the galvanizing process.

Preparation of the electrolyte and separator. The electrolyte was prepared by mixing 1.0 M $ZnSO_4$ and 0.1 M $MnSO_4$ in deionized water. The fatty alcohol solution, prepared as described above, was used for surface treatment of PP nonwoven fabrics. After the treatment, the treated PP fabric was immersed in the prepared electrolyte solution.

Characterization

The morphology and the chemical composition of MCS–PANi and Zn electrodes were characterised by scanning electron microscopy (SEM, Jeol JSM-6510LV) and energy-dispersive X-ray mapping analysis (EDX mapping). The phase and crystal structure of the MCS–PANi were characterized by X-ray diffractometry (Cu Kα irradiation, λ = 1.5406 Å). The XPS (Thermo Fisher) analysis was used to characterise the MCS–PANi cathode by using monochromatic Al Kα radiation (hm = 1486.6 eV). Electrochemical properties of MCS–PANi electrodes were studied with a Bio-Logic VSP-300 electrochemical station using a three-electrode configuration with a standard calomel electrode (SCE) as a reference electrode (RE), a Pt rod as a counter electrode (CE), the MCS–PANi electrode as working electrodes (WE) and electrolytes of $ZnSO_4$ 1 M–$MnSO_4$ 0.1 M. Regarding the performance test of a full-cell MPZHSC, a two-electrode electrochemical system was utilized. The electrochemical measurements including cyclic voltammetry (CV), galvanostatic charge/discharge (GCD), and electrochemical impedance spectroscopy (EIS) were conducted. Prior to electrochemical measurements, the electrode samples were immersed in the electrolyte solution for about 30 min.

Results and discussion

The preparation process of the MPZHSC is briefly illustrated in Scheme 1. First, the MCS–PANi composite (cathode) was directly grown on a graphite paper substrate by the electrodeposition to form a porous structure as reported previously.[39] Meanwhile, a metallic Zn-based electrode (anode) was prepared by the electroplating method using a mixture of fatty alcohol ethoxylate and $ZnSO_4$ solution as the electrolyte, resulting in the formation of a hierarchical micro-flower-like Zn structure. Subsequently, an MPZHSC was assembled by the MCS–PANi composite cathode, Zn anode, $ZnSO_4$/$MnSO_4$ electrolyte and nonwoven PP separator as shown in Scheme 1. The porous structure of both the cathode and anode contributes to the excellent electrochemical performance of the prepared ZHSC.

Characterisation of materials

Fig. 1(a)–(c) show the SEM images of the MCS–PANi cathode material at different magnifications. It can be seen that the cathode's surface is porous. It has small holes with a diameter of several μm interspersed with raised surrounding leaf scales on most of the electrode surface. This structure enhances the contact of the cathode with the electrolyte and as a consequence improves the effect of double layer charge and the participation of ions in redox reactions. In addition, the presence of aniline favors the adherence of the active MCS material to the substrate (*i.e.*, highly bonded large polyaniline arrays to the porous graphite substrate).

Fig. 1(d)–(f) show the micro-flower-like morphology on the surface of the Zn anode. The resulting petals have a thickness of around hundreds of nm that can reach the formation of two-dimensional nanosheets. Compared with the previous results,[36,39] the zinc nanosheets are more sparsely distributed

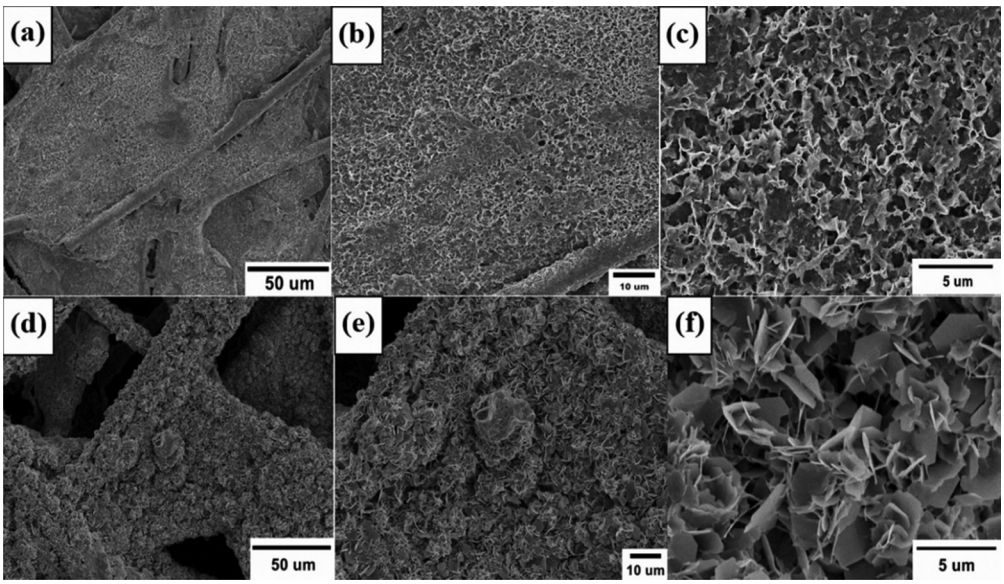

Fig. 1 SEM images at different magnifications of the MCS–PANi cathode (a)–(c) and Zn anode (d)–(f).

due to the interaction of fatty alcohols in the plating process and the isolation of zinc ions. Besides, during the operation of the Zn-ion hybrid supercapacitor, it is possible for the zinc electrode to undergo a chemical reaction that causes the formation of dendrites:

$$Zn + 4OH^- \leftrightarrow Zn(OH)_4^{2-} + 2e^- \leftrightarrow ZnO + 2OH^- + H_2O + 2e^-.$$

The presence of fatty alcohol molecules on the surface of zinc nanosheets limits the direct contact of zinc with water ions (OH^-).[36] It also reduces the oxidation, corrosion, gas generation as well as the growth of dendrites during the preparation and operation of MPZHSC.[31,35,36]

To clarify the actual material composition of the electrode, EDX and EDX mapping analyses were performed. Fig. 2 indicates the composition and elemental distribution of the MCS–PANi composite. The atomic percentage composition of the three elements Mn, Co, and S was 3.37, 3.45, and 4.44%, respectively. The nitrogen composition indicating the presence of PANi was 12.3% by atomic percentage. The presence of C element stems mainly from the porous graphite substrate. Along with that, there is uniform distribution of Mn, Co, S, and N elements on the entire survey surface.

The crystal phase, chemical element composition and oxidation states of cations on the surface of the sample were further evaluated by XRD and XPS techniques, respectively. The XRD pattern of the as-fabricated MCS/PANi electrode is shown in Fig. S2 (ESI†). It is observed that the intense diffraction peak around $2\theta = 26.5^\circ$ is due to the (002) plane of the graphite substrate. Two characteristic peaks at 20.3° and 25.5° belong to (020) and (200) crystal planes of PANi in its emeraldine salt form, respectively.[42,43] The well-defined diffraction peaks at about 30.8°, 31.4°, 38.3°, 50.2° and 55.3° are indexed to (311), (222), (400), (511) and (440) planes of the spinel $MnCo_2S_4$ structure, respectively (JCPDS card no: 73-1703), as observed in the previous report.[40,44] Besides, it can be seen that the peaks with low intensity at 35.4°, 47.0° and 54.7° correspond to the hexagonal CoS (JCPDS 65-3418).[45] In addition, no other peaks related to impurities were found.

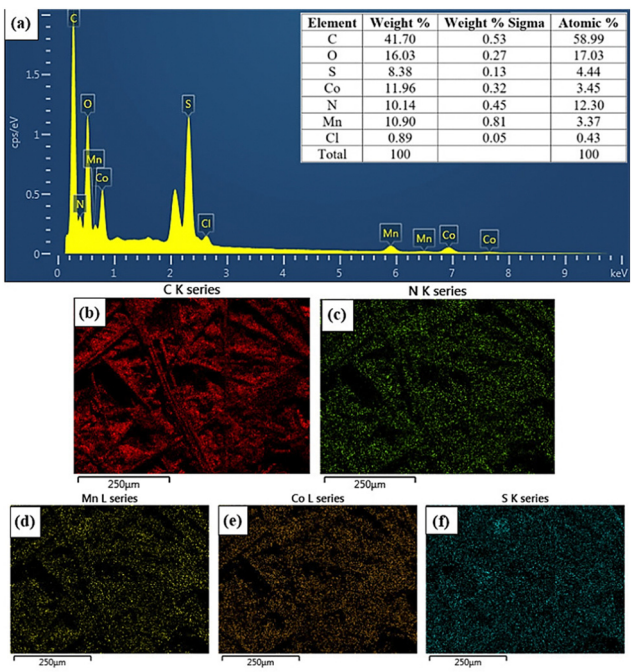

Fig. 2 EDX spectrum (a) and EDX mapping analysis (b)–(f) of the MCS–PANi composite material. The inset is the quantitative analysis of chemical composition of the sample.

The chemical composition and oxidation states of cations on the surface of the sample were further evaluated using the XPS technique.

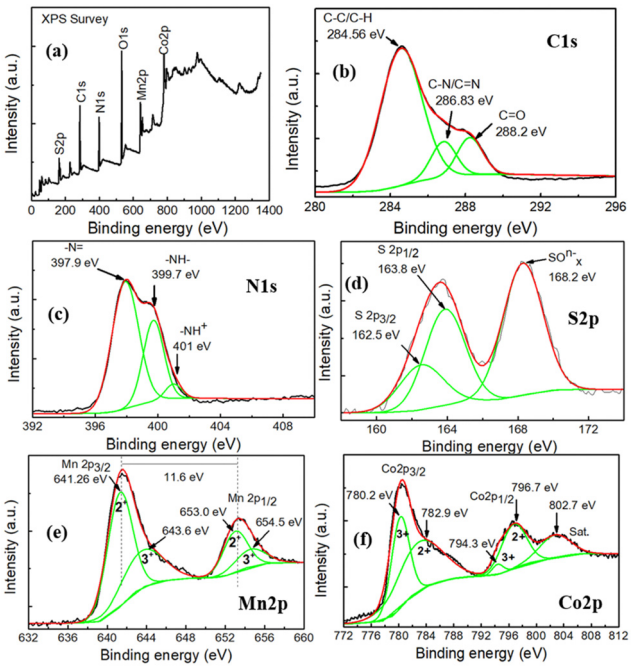

Fig. 3 Wide scan survey XPS spectrum of the MCS–PANi composite (a); high-resolution XPS spectra of C1s (b), N1s (c), S2p (d), Mn2p (e) and Co2p (f).

Fig. 3(a) shows the full XPS spectrum of the MCS–PANi composite, and Fig. 3(b)–(f) reveal high-resolution core-level XPS spectra of C 1s, N 1s, S 2p, Mn 2p and Co 2p, respectively. Fig. 3(b) shows the high-resolution C1s spectrum after using the Gaussian fitting method. The spectrum can be divided into three peaks, indicating the presence of benzene ring-C (C–C/C–H, 284.56 eV), C–N/C═N (286.83 eV), and C═O of quinoid (288.2 eV).[46] The high-resolution N 1s spectrum of PANi can be deconvoluted into three binding energy states, the peak of (═N–) at 397.9 eV, the peak of (–NH–) at 399.7 eV and the one of (–NH^+–) at 401 eV. The appearance of the 401 eV peak indicated that nitrogen species in PANI were protonated and interacted with the $MnCo_2S_4$ component in the PANI–$MnCo_2S_4$ composite.[47,48] The characteristic S 2p peaks at 162.5 and 163.8 eV belong to S $2p_{3/2}$ and S $2p_{1/2}$, respectively, which were assigned the typical characteristic of sulfur with metal ions (Co–S, Mn–S bonding).[49] Another peak was observed at 168.2 eV, which indicates the high oxide state of sulfur due to exposure to air and electrodeposition precursor salts.[49–52] As shown in Fig. 3(e), the Mn 2p spectrum also has two spin–orbit doublets, with Mn $2p_{3/2}$ located at 641.2 eV and Mn $2p_{1/2}$ located at 653.0 eV and co-existence of both Mn^{2+} and Mn^{3+} cations. The Mn 2p satellite separation is 11.6 eV. While the peaks at 641.26 eV and 653.0 eV correspond to oxidation sates of Mn^{2+}, the peaks at 643.6 eV and 654.5 eV are of the oxidation sates of Mn^{3+}. Fig. 3(f) presents the Co 2p core-level spectrum with two pairs of spin–orbit doublets, with Co $2p_{3/2}$ located at 780.2 eV and Co $2p_{1/2}$ at 796.7 eV. After using the Gaussian fitting method, the spectra can be divided into five peaks. Among them, two peaks at 780.2 eV and 794.3 eV correspond to the existence of Co^{3+} valence and two other peaks at 782.9 eV and 796.7 eV correspond to the existence of Co^{2+} valence. The satellite peak appears at 802.7 eV. These results match well with the reported data of Co 2p and Mn 2p spectra in $CoMn_2S_4$.[53] Therefore, the XRD and XPS results further confirmed the presence of Mn^{2+}, Mn^{3+}, Co^{2+}, Co^{3+} and PANi in the as-fabricated MCS/PANi cathode, which will play a role for the high electrochemical performance of electrode materials.

Electrochemical characterization

It was demonstrated that transition-metal sulfide materials typically achieve high specific capacitance values up to thousands of F g^{-1} in alkaline electrolyte solutions such as 6 M KOH electrolyte.[38,40,41,54–56] In the current study, the electrochemical performance of the MCS–PANi electrode alone in the $ZnSO_4$ 1 M–$MnSO_4$ 0.1 M electrolyte was evaluated. Fig. 4(a) shows CV curves at different scan rates from 5 to 50 mV s^{-1} over a wide potential range from −1 to 0.9 V. It can be seen that the MCS–PANi electrode still exhibits a high redox reactivity in the $ZnSO_4$ 1 M–$MnSO_4$ 0.1 M electrolyte. For all scan rates, prominent redox peaks appear at about 0.2 and 0.8 V. This demonstrates that the porous structure of the cathode allows the electrolyte ions to readily exchange and react with the electrode material even at high voltage reversal rates. Likewise, the GCD curves also show its nonlinear faradaic effect. The two shoulder-shaped platforms of the charge–discharge curve are relatively large and have a similar appearance location to the peaks of the CV curves at 0.2 V and 0.6 V (Fig. 4(b)). The inset of Fig. 4(b) shows more clearly the charge–discharge characteristics with a high current density of 30 and 40 A g^{-1}. The GCD curve at high current densities maintains its nonlinear appearance. From both the CV and GCD curves, it can be observed that the prepared MCS–PANi composite has excellent electrochemical properties and is suitable as the cathode for the Zn-ion hybrid supercapacitor. However, the Coulombic efficiency is not too high (the charge time is longer than the discharge time), and it is possible due to the fact that the electrolyte solution contains the fatty alcohol which partially affects the charge–discharge process.

For the full-cell MPZHSC, the CV curves retain similar shapes compared with those of the MCS–PANi positive electrode. In the current work, the sweep potential is up to 2 V. This potential window value is relatively high compared to those in previous studies on Zn-ion hybrid supercapacitors as well as aqueous Zn-ion batteries.[23–28,31–35,39] This will increase the energy storage capacity of the supercapacitor as the energy is proportional to the square of the potential. The CV and GCD curves in Fig. 4(c) and (d) exhibit redox peaks and nonlinearity, suggesting that the capacitance is attributed by the combination of pseudo-capacitance mechanisms.[40,41] The reaction mechanism in the anode using zinc ions can be formulated as eqn (1).[38]

$$Zn^{2+} + 2e^- \leftrightarrow Zn \quad (1)$$

Mn and Co are both multivalent transition metals and readily participate in reversible redox reactions. The fast faradaic

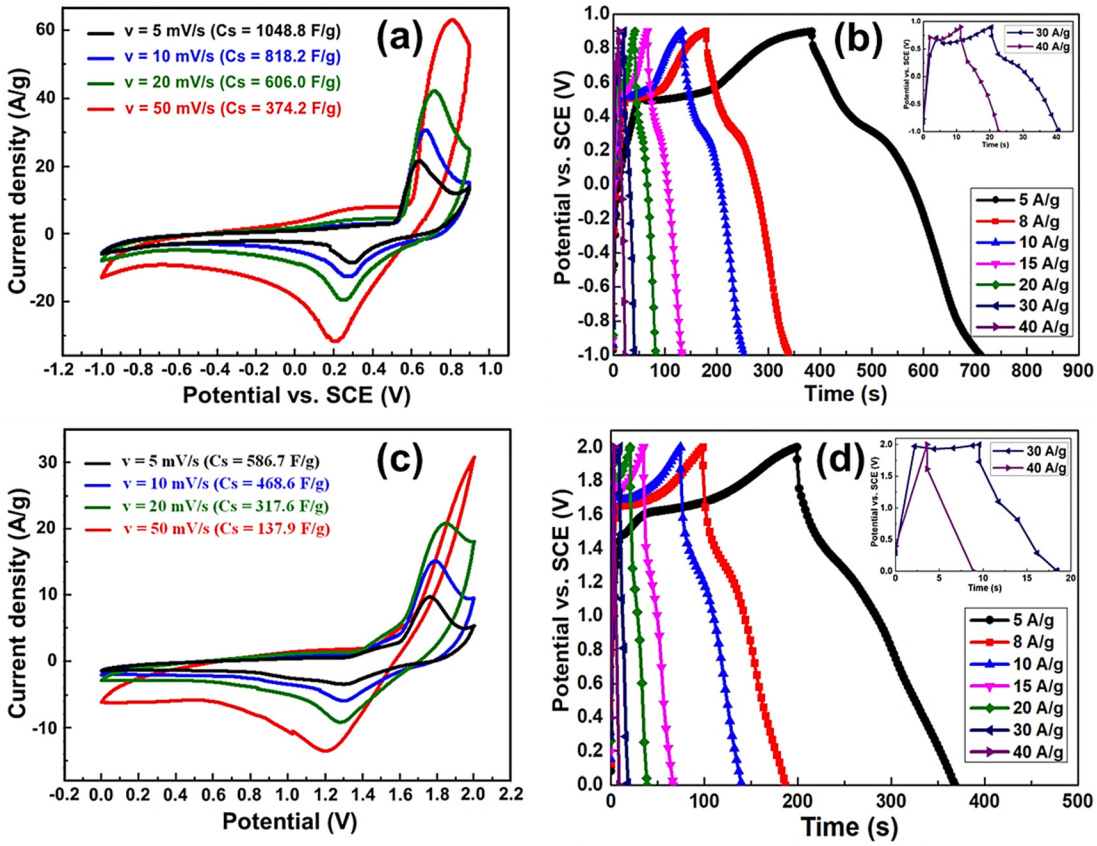

Fig. 4 CV and GCD curves of the MCS–PANi cathode (a), (b) and full-cell MPZHSC (c), (d) at different scan rates and current densities.

reactions are mainly due to the interaction of Mn and Co ions with the OH^-, and they are determined by the following equations:[57,58]

$$H_2O \leftrightarrow H^+ + OH^- \quad (2)$$

$$CoS + OH^- \leftrightarrow CoSOH + H_2O + e^- \quad (3)$$

$$CoSOH + OH^- \leftrightarrow CoSO + H_2O + e^- \quad (4)$$

$$MnS + OH^- \leftrightarrow MnSOH + e^- \quad (5)$$

$$MnSOH + OH^- \leftrightarrow MnSO + H_2O + e^- \quad (6)$$

A self-doping process possibly occurs in PANi. At the charged state, half of the nitrogen in the PANi chain is oxidized into the forms of $-NH^+-$, $-NH^+=$, or $-N=$. This enables PANi to react reversibly with SO_4^{2-} ions from electrolyte solutions, especially with $MnSO_4$.[59]

From the CV curves, the specific capacitances for the three-electrode system (MCS–PANi electrode) and the two-electrode system (full-cell MPZHSC) and the energy density are calculated according to the following formulas, respectively:

$$C_{sp} = \frac{S}{mv\Delta V}(F\ g^{-1}) \quad (7)$$

$$C'_{sp} = \frac{2S}{mv\Delta V}(F\ g^{-1}) \quad (8)$$

The highest obtained specific capacitance values at a CV scan rate of 5 mV s^{-1} are 1048.8 F g^{-1} for the MCS–PANi cathode and 586.7 F g^{-1} for the full-cell MPZHSC, as shown in Fig. 4(a) and (c). The high specific capacitances of the single electrode and the full-cell supercapacitor obtained indicate the high energy reserve of the MCS–PANi electrode material, and it is better than that of the recently published articles.[39,60,61] The working mechanism of the full-cell MPZHSC can be explained based on the reaction equations of (1)–(6). Here, OH^- ions are the main factor for the operation process. If OH^- ions are reacted with Zn, it will produce dendrites and reduce the durability and electrochemical quality of the supercapacitor. In the current study, the use of fatty alcohols to limit the reaction between Zn and OH^- will ensure that the reversible reactions of (1)–(6) take place smoothly and efficiently. In addition, PANi also has a self-doping mechanism thanks to the action of H^+ ions and SO_4^{2-} ions, which increases the electrochemical quality of the supercapacitor.[59]

To better characterize the performance of the MCS–PANi cathode, the electrochemical kinetics was investigated with the power law and Dunn method.[62] The equations used are as follows:

$$i = av^b \quad (9)$$

$$i(V) = k_1 v + k_2 v^{\frac{1}{2}} \quad (10)$$

Fig. S3a–c (ESI†) show the different values of coefficient b in eqn (9), determined for the redox peaks and some potential locations in the CV scan range. The b values obtained at both positive and negative redox peaks are approximately 0.5, demonstrating the diffusion-controlled faradaic characteristic. However, examining b at potential values in the CV measurement, b has a wide range of values and reaches the highest calculated values of 0.75 at (anodic) oxidation and 0.88 at reduction (cathodic). This proves that the process in the Zn-ion hybrid supercapacitor appears in both capacitive and diffuse processes. Therefore, eqn (10) is used to determine the % contribution of the two processes. Fig. S3c and d (ESI†) indicate the contribution ratio of the capacitive process. The capacitance contribution increased from 39% to 68% as the CV scan rate increased from 5 to 50 mV s^{-1} due to the insufficient adsorption/desorption time of OH^- ions onto/from the surface of the electrode material.[63] Table S1 (ESI†) provides different electrode materials along with fabrication methods and electrolyte solutions to compare with the electrochemical performance of the MCS–PANi electrode in the non-alkaline electrolyte solution.

The electrochemical impedance spectra were analyzed only for a two-electrode complete hybrid supercapacitor system consisting of the MCS–PANi cathode, the Zn-plated anode and the PP nonwoven separator that was hydrophilic-treated with $ZnSO_4$ (1 M)–$MnSO_4$ (0.1 M) electrolyte. Fig. 5(a) shows the EIS Nyquist plot of full-cell MCS–PANi-ZHSC. The inset in Fig. 5(a) shows the corresponding equivalent circuit model diagram (ECM), which includes an equivalent series resistance (R_s), a resistance for charge transfer at the electrode/electrolyte/separator interface (R_{CT}), a leakage resistance (R_L), two constant phase elements (CPE and CPE_L) of the non-ideal capacitor and a Warburg diffusion element (W) – representing the resistance of ionic diffusion in the electrolyte. The series resistance of the R_s system is 4.3 Ω, while the ion exchange resistance is 5.5 Ω. The resistance value is caused by the fatty alcohol wetting admixture together with the pore/surface structure of the non-wovens. The internal resistance of the full-cell MPZHSC and the charge–discharge current also affect the capacitance value when this device works. As shown in Fig. 5(b), the specific capacitance of the full-cell MPZHSC is only 390 F g^{-1} at a GCD current density of 5 A g^{-1}. The specific capacitance value tends to decrease gradually with the increase of the working current. This will generally affect the relationship between energy density and power density as shown in Fig. 5(c). The maximum energy density of the device achieves 216 W h kg^{-1} at a power density of 4610 W kg^{-1} and remains 47.5 W kg^{-1} at 32 264 W kg^{-1}. However, we have a very large leakage resistance (5.5 MΩ) that possibly helps the MPZHSC to reduce the self-discharge rate. Fig. 5(d) shows the cycling stability of the MPZHSC with a high charge/discharge current density of 50 A g^{-1}. The supercapacitor still maintains a very good durability of 98.3% of its initial capacity after 11 232 cycles (see more in Table S2, ESI† to compare the electrochemical qualities of some other ZHSCs).

To evaluate the self-discharge proccess of the full-cell MPZHSC, the device was charged to 2 V and the self-discharge

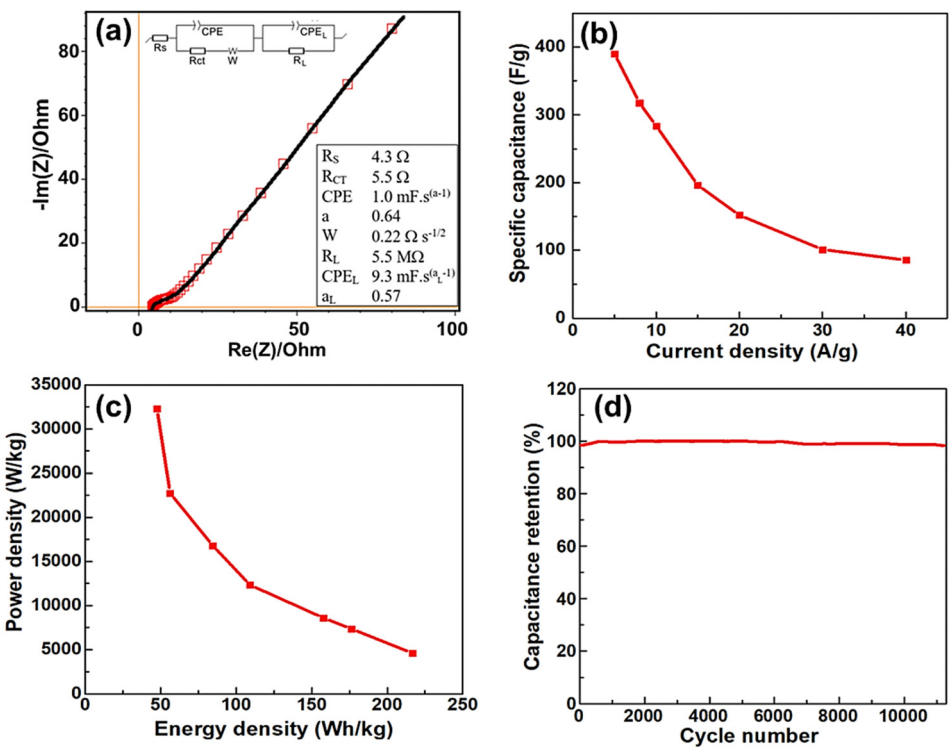

Fig. 5 EIS (a), effect of charge/discharge current density on specific capacitance (b), the relationship between energy density and power density (c) and cycling stability of the full cell MPZHSC after 11 232 charge–discharge cycles (d).

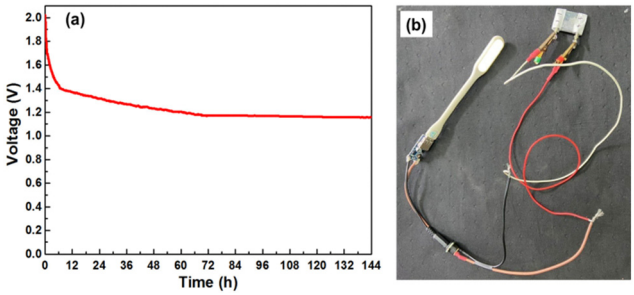

Fig. 6 (a) Self-discharge behavior of full-cell MPZHSC and (b) the full-cell MPZHSC device is lighting up a 2.5W-USB LED module.

rate was recorded by measuring the open-circuit voltage (OCV). In Fig. 6(a), the change in the OCV is observed to have two stages. In the first stage, the OCV drops quite quickly from 2 V to 1.4 V within about 7 hours. Then, it slowly decreased from 1.4 V to about 1.2 V after 137 hours in the second stage. Thus, after 7 days of the self-discharge, the device maintained 60% its initial voltage value and it is much higher than those of traditional supercapacitors.[64–68] The full-cell MPZHSC with a small active area of 2 cm^2 was also charged to 2 V and connected to a 2.5W USB LED module (Fig. 6(b)). The period of time when the LED was on until it turns off was about 15 min. Thus, the MPZHSC device demonstrated its high energy storage capacity.

Conclusion

The Mn–Co transition-metal sulfide–polyaniline composite material was successfully prepared as a cathode for a zinc-ion hybrid supercapacitor using a one-step reverse pulse electrodeposition method. The interesting results showed that the electrode achieved a high specific capacitance value in a non-alkaline electrolyte solution (1048.8 F g^{-1} at a scan rate of 5 mV s^{-1}). Fatty alcohol ethoxylate was used as a major additive in surface treatment of the non-woven PP separator and Zn cathode. A full-cell MPHZSC was also assembled. The device exhibited outstanding electrochemical behaviors such as a wide potential window of 2 V in the aqueous electrolyte, a high specific capacitance of 586.7 F g^{-1} at a scan rate of 5 mV s^{-1}, a high energy density of 216 W h kg^{-1}, and excellent cycling stability with over 98.3% of initial capacitance retention at a current density of 50 A g^{-1} after 11 232 charge–discharge cycles. The device also showed a low self-discharge rate by retaining over 60% of its initial voltage value after 7 days. A full-charged device was able to illuminate a 2.5 W LED module for about 15 min. We believe that this study not only provides good ideas for developing high-performance ZHSCs but also shows a potential perspective for the practical applications of ZHSCs.

Author contributions

DVT and DTT prepared electrochemical solutions, performed the electrodeposition/electroplating process and were major contributors in writing the manuscript. LTTT, NTD and NVT performed the analysis and assessment of the morphology and structure. PTN and NTTT performed the measurements and analyzed the electrochemical results. LTL and LTT designed the full cell of MPZHSC. DV and TKL worked on the manuscript. LTL and TDL helped to supervise the project and improved the manuscript. All the authors read and approved the final manuscript.

Conflicts of interest

The authors declare that they have no competing interests.

Acknowledgements

This work was supported by the Vietnam National Foundation for Science and Technology Development (NAFOSTED) under grant number 02/2020/TN.

References

1 M. Armand and J. M. Tarascon, *Nature*, 2008, **451**, 652.
2 D. Larcher and J. M. Tarascon, *Nat. Chem.*, 2015, **7**, 19–29.
3 X. Liu, Y. Li, X. Xu, L. Zhou and L. Mai, *J. Energy Chem.*, 2021, **61**, 104–134.
4 K. Chayambuka, G. Mulder, D. L. Danilov and P. H. L. Notten, *Adv. Energy Mater.*, 2020, **10**, 2001310.
5 N. Yabuuchi, K. Kubota, M. Dahbi and S. Komaba, *Chem. Rev.*, 2014, **114**, 11636–11682.
6 J. Mao, T. Zhou, Y. Zheng, H. Gao, H. K. Liu and Z. Guo, *J. Mater. Chem. A*, 2018, **6**, 3284–3303.
7 Q. Zhang, Z. Wang, S. Zhang, T. Zhou, J. Mao and Z. Guo, *Electrochem. Energy Rev.*, 2018, **1**, 625–658.
8 Z. Wang, X. Chu, Z. Xu, H. Su, C. Yan, F. Liu, B. Gu, H. Huang, D. Xiong, H. Zhang, W. Deng, H. Zhang and W. Yang, *J. Mater. Chem. A*, 2019, **7**, 8633.
9 M. E. Şahin, F. Blaabjerg and A. Sangwongwanich, *Energies*, 2022, **15**, 674.
10 C. Xu, B. Li, H. Du and F. Kang, *Angew. Chem., Int. Ed.*, 2012, **51**, 933.
11 D. Kundu, B. D. Adams, V. Duffort, S. H. Vajargah and L. F. Nazar, *Nat. Energy*, 2016, **1**, 16119.
12 O. Chusid, Y. Gofer, H. Gizbar, Y. Vestfrid, E. Levi, D. Aurbach and I. Riech, *Adv. Mater.*, 2003, **15**, 627–630.
13 T. Ichitsubo, T. Adachi, S. Yagi and T. Doi, *J. Mater. Chem.*, 2011, **21**, 11764–11772.
14 R. E. Doe, R. Han, J. Hwang, A. J. Gmitter, I. Shterenberg, H. D. Yoo, N. Pour and D. Aurbach, *Chem. Commun.*, 2014, **50**, 243–245.
15 A. L. Lipson, B. Pan, S. H. Lapidus, C. Liao, J. T. Vaughey and B. J. Ingram, *Chem. Mater.*, 2015, **27**, 8442–8447.
16 A. Ponrouch, C. Frontera, F. Bardé and M. R. Palacín, *Nat. Mater.*, 2016, **15**, 169–172.
17 M. Wang, C. Jiang, S. Zhang, X. Song, Y. Tang and H. M. Cheng, *Nat. Chem.*, 2018, **10**, 667–672.

18 M. C. Lin, M. Gong, B. Lu, Y. Wu, D. Y. Wang, M. Guan, M. Angell, C. Chen, J. Yang, B. J. Hwang and H. Dai, *Nature*, 2015, **520**, 324–328.
19 N. Jayaprakash, S. K. Das and L. A. Archer, *Chem. Commun.*, 2011, **47**, 12610–12612.
20 H. Chen, F. Guo, Y. Liu, T. Huang, B. Zheng, N. Ananth, Z. Xu, W. Gao and C. Gao, *Adv. Mater.*, 2017, **29**, 1605958.
21 L. D. Reed, S. N. Ortiz, M. Xiong and E. J. Menke, *Chem. Commun.*, 2015, **51**, 14397–14400.
22 C. Xu, Y. Chen, S. Shi, J. Li, F. Kang and D. Su, *Sci. Rep.*, 2015, **5**, 14120.
23 Y. Fu, Q. Wei, G. Zhang, X. Wang, J. Zhang, Y. Hu, D. Wang, L. Zuin, T. Zhou, Y. Wu and S. Sun, *Adv. Energy Mater.*, 2018, **8**, 1801445.
24 D. Selvakumaran, A. Pan, S. Liang and G. Cao, *J. Mater. Chem. A*, 2019, **7**, 18209–18236.
25 N. Zhang, F. Cheng, J. Liu, L. Wang, X. Long, X. Liu and F. Li, *Nat. Commun.*, 2017, **8**, 405.
26 L. Su, L. Liu, Y. Wang, Y. Lu and X. Yan, *Chin. Chem. Lett.*, 2020, **31**, 2358–2364.
27 Z. M. Pan, Z. M. Lu, L. Xu and D. W. Wang, *Appl. Surf. Sci.*, 2020, **510**, 145384.
28 X. S. Zhang, Z. X. Pei, C. J. Wang, Z. W. Yuan, L. Wei, Y. Q. Pan, A. Mahmood, Q. Shao and Y. Chen, *Small*, 2019, **15**, 1903817.
29 T. Ni, S. L. Wang, J. J. Shi, X. Y. Du, Q. H. Cheng, Z. Y. Dong, L. M. Ruan, W. Zeng, X. H. Guo, X. G. Ren and Z. X. Huang, *Adv. Mater. Technol.*, 2020, **5**, 2000268.
30 H. C. He, J. C. Lian, C. M. Chen, Q. T. Xiong and M. Zhang, *Chem. Eng. J.*, 2021, **421**, 129786.
31 C. Shen, X. Li, N. Li, K. Xie, J.-G. Wang, X. Liu and B. Wei, *ACS Appl. Mater. Interfaces*, 2018, **10**, 25446–25453.
32 W. Li, K. Wang, M. Zhou, H. Zhan, S. Cheng and K. Jiang, *ACS Appl. Mater. Interfaces*, 2018, **10**, 22059–22066.
33 K. Zhao, C. Wang, Y. Yu, M. Yan, Q. Wei, P. He, Y. Dong, Z. Zhang, X. Wang and L. Mai, *Adv. Mater. Interfaces*, 2018, **5**, 1800848.
34 L. Kang, M. Cui, F. Jiang, Y. Gao, H. Luo, J. Liu, W. Liang and C. Zhi, *Adv. Energy Mater.*, 2018, **8**, 1801090.
35 H. Li, C. Xu, C. Han, Y. Chen, C. Wei, B. Li and F. Kang, *J. Electrochem. Soc.*, 2015, **162**, A1439.
36 K. E. K. Sun, T. K. A. Hoang, T. N. L. Doan, Y. Yu, X. Zhu, Y. Tian and P. Chen, *ACS Appl. Mater. Interfaces*, 2017, **9**, 9681–9687.
37 K. E. K. Sun, T. K. A. Hoang, T. N. L. Doan, Y. Yu and P. Chen, *Chem. – Eur. J.*, 2018, **24**, 1667–1673.
38 D. T. Tung, L. T. T. Tam, H. T. Dung, N. T. Dung, P. N. Hong, H. M. Nguyet, N. Van-Quynh, N. V. Chuc, V. Q. Trung, L. T. Lu and P. N. Minh, *Electrochim. Acta*, 2021, **392**, 138992.
39 D. T. Tung, H. M. Nguyet, N. T. Dung, H. T. Dung, N. T. Yen, N. B. Thanh, P. N. Hong, P. V. Hoi, N. V. Quynh, P. N. Minh and L. T. Lu, *J. Electron. Mater.*, 2021, **50**, 4407–4414.
40 H. M. Nguyet, L. T. T. Tam, D. T. Tung, N. T. Yen, H. T. Dung, N. T. Dung, P. N. Hong, L. A. Tuan, P. N. Minh and L. T. Lu, *New J. Chem.*, 2022, **46**, 13996–14003.
41 L. T. T. Tam, D. T. Tung, H. M. Nguyet, N. T. N. Linh, N. T. Dung, N. V. Quynh, N. V. Dang, D. Vernardou, T. K. Le, L. A. Tuan, P. N. Minh and L. T. Lu, *RSC Adv.*, 2022, **12**, 20182.
42 J. Yan, T. Wei, B. Shao, Z. Fan, W. Z. Qian and M. Zhang, *Carbon*, 2010, **48**, 487–493.
43 Y. Zhang, J. Liu, Y. Zhang, J. Liu and Y. Duan, *RSC Adv.*, 2017, **7**, 54031–54038.
44 K. V. G. Raghavendra, C. V. V. M. Gopi, R. Vinodh, S. S. Raob, I. M. Obaidatc and H.-J. Kim, *J. Energy Storage*, 2020, **27**, 101159.
45 D. Ma, B. Hu, W. Wu, X. Liu, J. Zai, C. Shu, T. T. Tsega, L. Chen, X. Qian and T. L. Liu, *Nat. Commun.*, 2019, **10**, 3367.
46 B. Mu, W. B. Zhang, S. J. Shao and A. Q. Wang, *Phys. Chem. Chem. Phys.*, 2014, **16**, 7872–7880.
47 G. P. Pandey and A. C. Rastogia, *ECS Trans.*, 2013, **50**(43), 71.
48 M. Li, W. Yin, X. Han and X. Chang, *J. Solid State Electrochem.*, 2016, **20**, 1941–1948.
49 Y. Zhu, H. Chen, S. Chen, C. Li, M. Fan and K. Shu, *J. Mater. Sci.*, 2018, **53**, 6157–6169.
50 H. Fan, Y. Ma, W. Chen, Y. Tang, L. Li and J. Wang, *J. Alloys Compd.*, 2022, **894**, 162533.
51 H. S. Jadhav, A. Roy, G. M. Thorat, W.-J. Chung and J. G. Seo, *J. Ind. Eng. Chem.*, 2019, **71**, 452.
52 X. Ma, W. Zhang, Y. Deng, C. Zhong, W. Hua and X. Han, *Nanoscale*, 2018, **10**, 4816–4824.
53 X. Lv, Z. Zhou, X. Liao, Z. Liu, L. Feng, X. Lin and Y. Ni, *J. Alloys Compd.*, 2022, **896**, 163024.
54 F. Zhang, M. Cho, T. Eom, C. Kang and H. Lee, *Ceram. Int.*, 2019, **45**, 20972–20976.
55 A. M. Elshahawy, X. Li, H. Zhang, Y. Hu, K. H. Ho, C. Guan and J. Wang, *J. Mater. Chem. A*, 2017, **5**, 7494–7506.
56 Y. M. Chen, Z. Li and X. W. D. Lou, *Angew. Chem., Int. Ed.*, 2015, **127**, 10667–10670.
57 H. Liu, Z. Li, Z. Yao, Y. Liu, Q. Zhang, Y. Sun and Z. Li, *J. Colloid Interface Sci.*, 2019, **551**, 119–129.
58 S. S. Haider, M. Z. Iqbal, S. Zakar, A. M. Afzal, K. Yaqoob and S. Aftab, *J. Energy Storage*, 2021, **39**, 102608.
59 H. Y. Shi, Y. J. Ye, K. Liu, Y. Song and X. Sun, *Angew. Chem., Int. Ed.*, 2018, **130**, 16597–16601.
60 P. Zhang, Y. Li, G. Wang, F. Wang, S. Yang, F. Zhu, X. Zhuang, O. G. Schmidt and X. Feng, *Adv. Mater.*, 2019, **31**, 1806005.
61 Z. Pan, Z. Lu, L. Xu and D. Wang, *Appl. Surf. Sci.*, 2020, **510**, 145384.
62 X. Liu, Y. Liu, X. Yan, J.-L. Lan, Y. Yua and X. Yanga, *Mater. Chem. Front.*, 2019, **3**, 120–126.
63 Y. Wang, C. Xiang, Y. Zou, F. Xu, L. Sun and J. Zhang, *J. Energy Storage*, 2021, **41**, 102838.
64 A. M. Oickle, J. Tom and H. A. Andreas, *Carbon*, 2016, **110**, 232–242.
65 L. García-Cruz, P. Ratajczak, J. Iniesta, V. Montiel and F. Béguin, *Electrochim. Acta*, 2016, **202**, 66–72.
66 M. A. Davis and H. A. Andreas, *Carbon*, 2018, **139**, 299–308.
67 J. Menzel, E. Frąckowiak and K. Fic, *Electrochim. Acta*, 2020, **332**, 135435.
68 Q. Yang, Z. Huang, X. Li, Z. Liu, H. Li, G. Liang, D. Wang, Q. Huang, S. Zhang, S. Chen and C. Zhi, *ACS Nano*, 2019, **13**, 8275–8283.